

Chapter 2

The Pioneer Anomaly and Thermal Effects in Spacecraft

2.1 General Background

The twin Pioneer 10 and Pioneer 11 deep-space probes were launched, respectively, on March 3, 1972 and April 6, 1973 as part of NASA's Pioneer program of planetary exploration. They were the first human objects to venture beyond the asteroid belt and provided invaluable scientific data from their visits to Jupiter and Saturn, including some of the first close up photographs of these planets, like those shown in Fig. 2.1 [1, 2].

The general configuration of these deep-space probes can be seen in Fig. 2.2 [3]. There is a main equipment compartment located directly behind the high-gain antenna, and two Radioisotope Thermal Generators (RTGs) mounted on two structures extending from the main compartment.

The scientific objectives of Pioneer 10 and 11 included the study of the interplanetary and planetary magnetic fields, solar wind parameters, cosmic rays, transition region of the heliosphere, neutral hydrogen abundance, and the atmosphere of Jupiter, Saturn and some of their satellites [4].

Pioneer 10 would become the first man-made object, by some definitions, to leave the solar system. The last time Pioneer 10 made contact with Earth was on January 23, 2003, from a distance of more than 80 AU. Communications with Pioneer 11 had already ceased after September 30, 1995. The two Pioneer probes currently follow hyperbolic trajectories away from the Solar System in approximately opposite directions [4], as shown in Fig. 2.3.

The success of these missions would pave the way for the heavier and more sophisticated Voyager 1 and 2 missions a few years later, that would repeat the visits to Jupiter and Saturn and be the first to make Uranus and Neptune flybys.

Through the later stages of the Pioneer 10 and 11 missions, the analysis of the radiometric data began to reveal the presence of an anomalous acceleration in the approximate direction of the Sun. The existence of this acceleration, that became known as the *Pioneer anomaly*, was first reported in 1998 in a paper by Anderson



Fig. 2.1 Closeup pictures of Jupiter and Saturn taken, respectively, by Pioneer 10 and Pioneer 11 [1, 2]

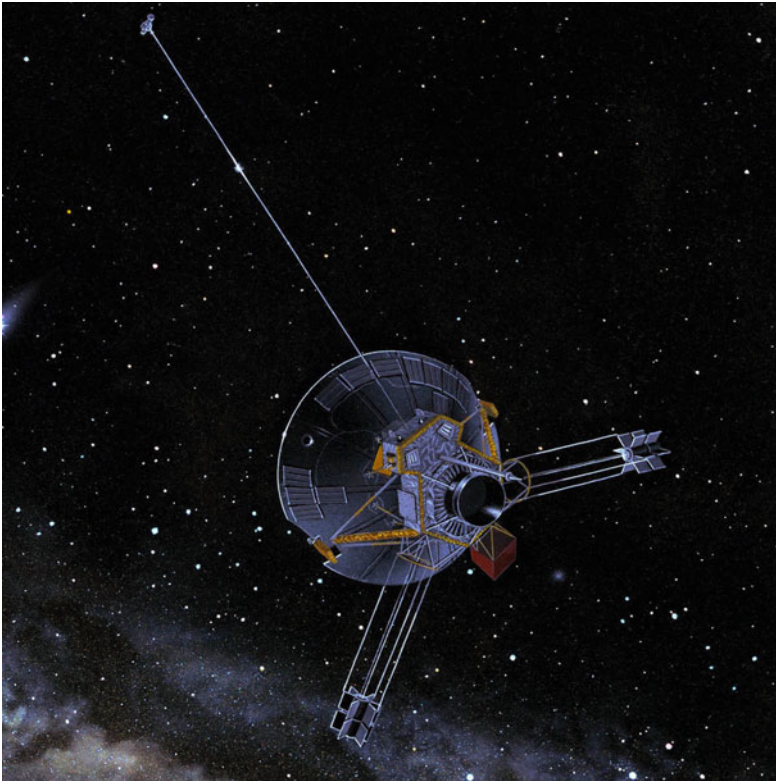


Fig. 2.2 Artist's impression of one of the Pioneers heading into deep space [3]. The main components are clearly visible: the two RTGs and the main equipment compartment behind the main parabolic antenna

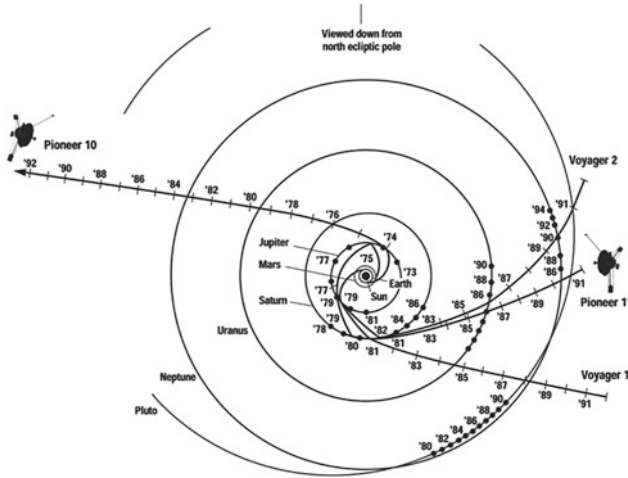


Fig. 2.3 Ecliptic pole view of Pioneer 10 and 11 and Voyager 1 and 2 trajectories. Taken from Ref. [5]

et al. [6]. The initial results pointed towards a constant value $a_{\text{Pioneer}} = (8.74 \pm 1.33) \times 10^{-10} \text{ m/s}^2$.

The possibility of thermal effects being responsible for this anomaly was raised early in the debate about its cause in two comments to the initial Anderson et al. paper. In his comment, Murphy drew attention to the fact that waste heat from the electronic equipment was radiated from the spacecraft through a set of louvered radiators located on the side that faced away from the Sun and estimated that this would generate an acceleration between 3.2×10^{-10} and $8.5 \times 10^{-10} \text{ m/s}^2$ [7]. Katz, on the other hand, mentioned that thermal radiation from the RTGs and scattered from the back of the antenna would be preferably directed away from the Sun, leading to a sunward acceleration [8]. Both argued, albeit on a qualitative basis, that thermal effects could provide significant clues for the unexplained acceleration.

In the more detailed study of the Pioneer anomaly that was presented by Anderson et al. in 2002, the thermal hypothesis was precluded. The authors asserted that RTG and electrical power would have decreased significantly in the observed period due to the fact that the primary power source was Plutonium-238, an isotope with a half-life of 87.7 years. This was not compatible with an acceleration that appeared from the Doppler data to be constant, as shown in Fig. 2.4. Furthermore, their initial assessment of systematic error sources indicated that any acceleration arising from heat dissipation would be too small to account for the Pioneer anomaly [5] (see also Ref. [9]).

Soon afterwards, a paper by Scheffer came out with a qualitative estimate of the thrust available from the different heat sources onboard the Pioneer spacecraft [10]. A breakdown of different effects was presented, each with the available power and an efficiency factor that represents the portion of this power that is converted into

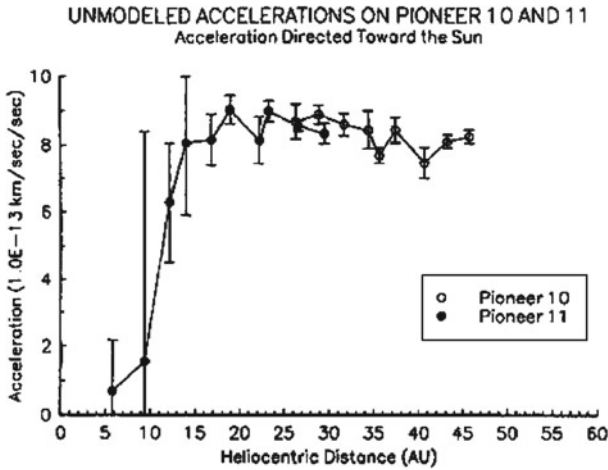


Fig. 2.4 Plot of the unmodelled accelerations of Pioneer 10 and 11, taken from Ref. [5]. Earlier data points do not represent true measurements, since they are masked by a large solar radiation force

Table 2.1 Scheffer’s estimate of available thrust from different sources in terms of equivalent directed power, as shown in Ref. [10]

Source of effect	Total power (W)	Efficiency	Thrust (W)	Decay (%/year)
Radiation from RHUs	8	0.5	4	0.78
Antenna shadow	25	0.3	7.5	0.68
Antenna radiate	25	0.6	15	0.68
RTG asymmetry	2000	0.009	18	0.68
Feed pattern	0.8	0.7	0.6	0
Radio beam	7.2	−1	−7.2	0
Radiation, main bus	59	0.54	32	cf. Ref. [10]
Radiation, instruments	1	0.1	0.1	cf. Ref. [10]
Total			70	

thrust, as shown in Table 2.1, taken from Ref. [10]. The author estimated that 58 W of power directed away from the sun would be enough to account for the anomalous acceleration, while estimating a total available thrust of 70 W, thus concluding that it was likely that the whole effect could be explained without the need for new physics.

As this debate went on, numerous attempts were made to explain the Pioneer anomaly through new physics. A large array of proposals were made, ranging from scalar fields in the context of braneworld models [11]; theories of gravity with scalar, tensor and vector components [12], post-Einsteinian metric extensions of General

Relativity (GR) [13] to theories of gravity with non-minimal coupling between matter and curvature [14]. The first two of these are summarised in Sect. 2.2 as illustrative examples. A more complete review of the different proposals can be found in Ref. [15], including unsuccessful attempts to explain the anomaly resorting to more conventional physics, like the gravitational pull of the Kuiper Belt [16].

The crucial issue of the anomaly's time signature remained controversial for quite some time. The first independent confirmation of the existence of the anomaly was presented in an unpublished paper by Markwardt, where his own analysis tools were used [17]. The best fit obtained from the Doppler data was a constant acceleration of $(8.60 \pm 1.34) \times 10^{-10} \text{ m/s}^2$. However, the author pointed out that this result was also statistically compatible with the time signature of the radioactive decay of the Plutonium-238 powering the RTGs and, as a consequence, a relation between the anomalous acceleration and heat dissipation could not be excluded.

At least two other independent Doppler data processing efforts were performed, one by Levy et al. [18] and another by Toth [19], further reinforcing confidence on the existence of a Pioneer anomaly. Besides both confirming the existence of a constant component with values similar to the previously reported, the former focuses its analysis on short time-scale periodic accelerations, while the latter includes the estimate of a “jerk” term (time derivative of the acceleration), finding it to be consistent with the expected temporal variation of a recoil force due to heat generated on board and emitted anisotropically [19].

The issue was finally settled in a paper co-authored by Turyshev, a member of the team at the Jet Propulsion Laboratory (JPL) that originally put forward the existence of the anomaly, with the collaboration of Markwardt, Ellis and Toth. The results supported a time-decaying acceleration compatible with a thermal origin to the anomaly [20]. The tracking data was fitted to constant, linear and exponential models with the latter having the smaller residuals, as summarised in Table 2.2 and Fig. 2.5 [20].

At this point, it had long become clear that a reliable quantitative description of the effects of Pioneer's thermal emissions was essential. In response to this need, three independent studies were carried out in the last few years by scientific teams working in Portugal, Germany and the United States.

Table 2.2 Pioneer 10 and 11 acceleration fits to constant, linear, and exponential models, as reported in Ref. [20]

Spacecraft	Model	σ_p (mHz)	$a_p(t_0)$ (10^{-10} m/s^2)	\dot{a}_p ($\text{m/s}^2/\text{year}$)	β^{-1} (year)
Pioneer 10	Constant	4.98	8.17	–	–
	Linear	4.60	11.06	–0.17	–
	Exponential	4.58	12.22	–	28.8
Pioneer 11	Constant	3.67	9.15	–	–
	Linear	2.09	11.65	–0.18	–
	Exponential	2.06	13.79	–	24.6

σ_p are the root mean square residuals, $a_p(t_0)$ is the acceleration on January 1, 1972, \dot{a}_p is the slope in the linear model and β^{-1} is the half-life in the exponential model

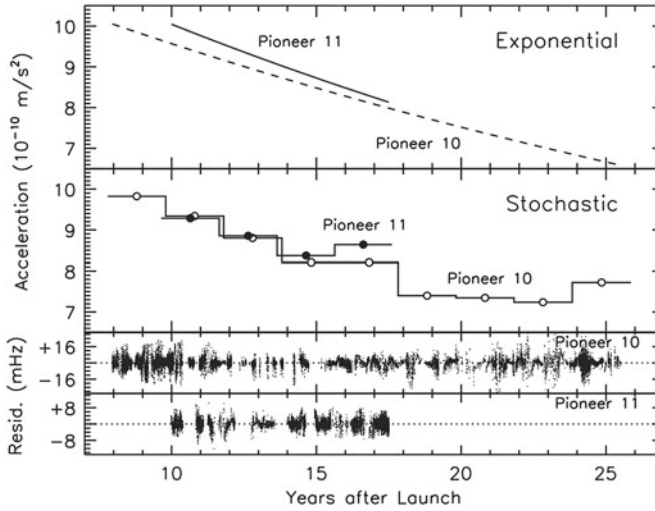


Fig. 2.5 *Top panel* Estimates of the anomalous acceleration of Pioneer 10 (*dashed line*) and Pioneer 11 (*solid line*) using an exponential model. *Second panel* Stochastic acceleration estimates for Pioneer 10 (*open circles*) and Pioneer 11 (*filled circles*), shown as step functions. *Bottom two panels* Doppler residuals of the stochastic acceleration model. Note the difference in vertical scale for Pioneer 10 versus Pioneer 11, show that Pioneer 10 data is much noisier. Taken from Ref. [20]

This chapter of the thesis sums up the work made by the Portuguese team in tackling this problem. The first results appeared in 2008, indicating that up to 67 % of the acceleration was explainable through thermal effects [21]. The results were obtained using a novel method based on a distribution of point-like radiation sources, that was thoroughly tested to ensure its reliability and conformity with the objectives that were set out [21, 22]. In order to provide a full description of the physics involved, the method was subsequently extended to include the modelling of reflections [23], as explored in detail in Sect. 2.3.

As we shall see, the approach chosen by our team allowed for the first complete and reliable determination of the thermal acceleration aboard the Pioneer and to conclude that they were, in fact, responsible for the Pioneer anomaly [23].

The results were subsequently confirmed by the German team working at the Center for Applied Space Technology and Microgravity (ZARM) in Bremen [24] and, finally, by the American team at the JPL [25], both using more conventional finite-element models.

2.2 New Physics Proposals

Out of the many attempts to explain the Pioneer anomaly through new physics, we briefly explore two illustrative examples of the kind of proposals that were put forward.

2.2.1 Scalar Field

One possible way to look at the problem of the Pioneer anomaly is in the context of a braneworld scenario, as done by Bertolami and Páramos [11]. In braneworld theories, our Universe is assumed to be a 4-dimensional membrane embedded in a higher dimensional bulk space.

The authors first attempt to use a Randall-Sundrum braneworld model and explain the Pioneer anomaly as an influence of the radion field, a scalar perturbation of the metric related to relative motion of the two branes. The authors conclude that this approach is unsuitable to provide the desired explanation.

A more promising possibility can arise from the presence of a scalar field ϕ with a potential $V(\phi) \propto -\phi^{-\alpha(r)}$, with $\alpha > 0$. This field is similar to the form a supergravity inspired quintessence field assumes in braneworld theories, but with the sign reversed.

The effect appears in the metric $g_{\mu\nu}$ as a small perturbation $h_{\mu\nu}$ to the Minkowsky metric $\eta_{\mu\nu}$, so that

$$g_{\mu\nu} = \eta_{\mu\nu} + h_{\mu\nu}. \quad (2.1)$$

The Lagrangian density \mathcal{L}_ϕ of the scalar field takes the form

$$\mathcal{L}_\phi = \frac{1}{2}\eta_{\mu\nu}\partial_\mu\phi\partial^\nu\phi - V(\phi). \quad (2.2)$$

Since this is a spherically symmetric problem, the formulation can be developed in spherical coordinates. Hence, Eq. (2.2) takes the form

$$\mathcal{L}_\phi = \frac{1}{2}\eta_{rr}(\phi')^2 - A^2\phi^{-\alpha}, \quad (2.3)$$

where A is a constant. The equation of motion of the scalar field is

$$\square^2\phi + \frac{dV(\phi)}{d\phi} = 0, \quad (2.4)$$

where $\square = \partial_\mu\partial^\mu$ is the d'Alembertian operator. This equation has as a solution in spherical coordinates

$$\phi(r) = \left((2 + \alpha)\sqrt{\frac{\alpha}{8 + \alpha}}Ar \right)^{\frac{2}{2+\alpha}} \equiv \beta^{-1}r^{\frac{2}{2+\alpha}}. \quad (2.5)$$

This means that the potential takes the form

$$V(\phi(r)) = -A^2\beta^\alpha r^{-\frac{2}{2+\alpha}}, \quad (2.6)$$

while the gradient term becomes

$$\frac{1}{2}(\phi'(r))^2 = A \left(\frac{\alpha}{4 + \alpha} \right) \beta^\alpha r^{-\frac{2\alpha}{2+\alpha}}. \quad (2.7)$$

The Lagrangian density in the Newtonian limit is given by

$$\mathcal{L}_\phi = -\frac{4}{4 + \alpha} V(\phi). \quad (2.8)$$

The energy-momentum tensor for the scalar field is given by the expression

$$T_{\mu\nu} = \partial_\mu \phi \partial_\nu \phi - \eta_{\mu\nu} \mathcal{L}_\phi. \quad (2.9)$$

This is then introduced in the linearised form of Einstein's equation

$$\frac{1}{2} \nabla^2 h_{\mu\nu} = 8\pi G \left(T_{\mu\nu} - \frac{1}{2} \eta_{\mu\nu} T \right), \quad (2.10)$$

where G is the gravitational constant. From the solution of this equation, one can obtain the radial acceleration caused by the scalar field

$$a_r = -\frac{C}{r^2} + (2 + \alpha) A^2 8\pi G \beta^\alpha r^{-\frac{2\alpha}{2+\alpha}} \left(\frac{C}{2} - \frac{r}{6 + \alpha} \right), \quad (2.11)$$

where C is a constant.

For $\alpha = 2$ one gets an expression for the acceleration that is compatible with the main constant observational signature of the Pioneer Anomaly:

$$a_r = -\frac{C}{r^2} + \sqrt{\frac{3}{2}} A^2 2\pi G + \sqrt{\frac{3}{2}} \frac{AC 8\pi G}{r}. \quad (2.12)$$

The first term represents the Newtonian contribution and the term proportional to r^{-1} is much smaller than the constant term for $4C/r \ll 1$, that is for $r \gg 6$ km, and is also much smaller than the Newtonian acceleration for $r \ll 2.9 \times 10^{22}$ km ≈ 100 Mpc, clearly covering the desired range. The constant term can, therefore, be identified with the anomalous acceleration by setting the constant A appropriately, for instance, if $a_{\text{Pioneer}} = 8.5 \times 10^{-10}$ m/s² then $A = 4.7 \times 10^{42}$ m⁻³ [11].

2.2.2 Scalar-Tensor-Vector Gravity

Another proposal was put forward by Brownstein and Moffat using Scalar-Tensor-Vector Gravity (STVG) theory to obtain an effect that fits the available data. The

theory is outlined in Ref. [12] and postulates the existence of a spin-1 vector field ϕ . Furthermore, in this theory the gravitational constant G , the vector field coupling strength ω and the vector field mass $\mu = 1/\lambda$ are all treated as scalar fields with their own dynamics. The action for STVG takes the form

$$S = \int dx^4 \sqrt{-g} (\mathcal{L}_{\text{Grav}} + \mathcal{L}_\phi + \mathcal{L}_S), \quad (2.13)$$

where g is the determinant of the metric. This action includes the Lagrangian densities for the vector field

$$\mathcal{L}_\phi = \omega \left(\frac{1}{4} (\partial^\mu \phi^\nu - \partial^\nu \phi^\mu) (\partial_\mu \phi_\nu - \partial_\nu \phi_\mu) + V(\phi) \right), \quad (2.14)$$

for the scalar quantities G , ω and μ

$$\begin{aligned} \mathcal{L}_S = & \frac{1}{G^3} \left(\frac{1}{2} g^{\mu\nu} \nabla_\mu G \nabla_\nu G + V(G) \right) \\ & + \frac{1}{G} \left(\frac{1}{2} g^{\mu\nu} \nabla_\mu \omega \nabla_\nu \omega + V(\omega) \right) \\ & + \frac{1}{\mu^2 G} \left(\frac{1}{2} g^{\mu\nu} \nabla_\mu \mu \nabla_\nu \mu + V(\mu) \right) \end{aligned} \quad (2.15)$$

and for gravitation

$$\mathcal{L}_{\text{grav}} = \frac{1}{16\pi G} (R + 2\Lambda), \quad (2.16)$$

where R is the scalar curvature and Λ is the cosmological constant.

From the development of the field equations, the equations of motion for a static spherically symmetric field about a central mass M can be obtained. The line element is written in spherical coordinates as

$$ds^2 = \gamma(r) dt^2 - \alpha(r) dr^2 - r^2 (d\theta^2 + \sin^2 \theta d\varphi^2). \quad (2.17)$$

An exact solution for the spherically symmetric static field equations can be obtained if the potential $V(\phi)$ and Λ are small enough to be neglected, yielding

$$\gamma(r) = 1 - \frac{2GM}{r} + \frac{Q^2}{r^2}, \quad \alpha(r) = 1 - \frac{2GM}{r} + \frac{Q^2}{r^2}, \quad (2.18)$$

where the charge ϵ of the spin-1 vector particle is taken into account in the quantity

$$Q = 4\pi G \omega \epsilon^2. \quad (2.19)$$

That can be compared to the usual Schwarzschild solution

$$\gamma_{\text{Schwarz}}(r) = 1 - \frac{2GM}{r}, \quad \alpha_{\text{Schwarz}}(r) = \frac{1}{1 - \frac{2GM}{r}}. \quad (2.20)$$

We can easily see that, as expected, for large values of r the STVG solution degenerates in the Schwarzschild solution. With some more manipulation, described in detail in Ref. [12], we finally obtain the equation of motion of a particle around a mass M

$$\frac{d^2 r}{dt^2} - \frac{J_N^2}{r^3} + \frac{GM}{r^2} = K \frac{e^{-\mu r}}{r^2} (1 + \mu r). \quad (2.21)$$

where J_N is the Newtonian orbital angular momentum and K is a positive quantity. Following the formulation developed in Ref. [12], the radial acceleration can be written as

$$a(r) = -\frac{G_\infty M}{r^2} + K(r) \frac{e^{-r/\lambda(r)}}{r^2} \left(1 - \frac{r}{\lambda(r)}\right). \quad (2.22)$$

The value for the gravitational constant appears renormalized as

$$G_\infty = G_0 (1 + \alpha_\infty), \quad (2.23)$$

where G_0 here denotes the Newtonian gravitational constant. The value for K is chosen as

$$K(r) = G_0 M \alpha(r). \quad (2.24)$$

Using Eq. (2.24), we can finally write the variation of G with distance to the central mass

$$G(r) = G_0 \left[1 + \alpha(r) \left[1 - e^{-r/\lambda(r)} \left(1 - \frac{r}{\lambda(r)} \right) \right] \right] \quad (2.25)$$

and the acceleration

$$a(r) = -\frac{G(r)M}{r^2}. \quad (2.26)$$

The authors then postulate that the Pioneer Anomaly is caused by the difference between the Newtonian gravitational constant G_0 and the new dynamic value $G(r)$. The anomalous Pioneer acceleration would thus be given by

$$a_{\text{Pio}} = -\frac{\Delta G(r) M_\odot}{r^2}, \quad (2.27)$$

where

$$\Delta G(r) = G(r) - G_0 = G_0 \left[\alpha(r) \left[1 - e^{-r/\lambda(r)} \left(1 - \frac{r}{\lambda(r)} \right) \right] \right]. \quad (2.28)$$

The proposed parametric representations for $\alpha(r)$ and $\lambda(r)$ are:

$$\alpha(r) = \alpha_{\infty} (1 - e^{\frac{r}{\bar{r}}})^{\frac{b}{2}}, \quad (2.29)$$

$$\lambda(r) = \frac{\lambda_{\infty}}{(1 - e^{\frac{r}{\bar{r}}})^b}. \quad (2.30)$$

Here, \bar{r} is a non-running distance scale parameter and b is a constant.

Using a least-squares routine, the authors obtain values for the constant parameters that yield the best fit to the acceleration residuals:

$$\alpha_{\infty} = (1.00 \pm 0.02) \times 10^{-3}, \quad (2.31)$$

$$\lambda_{\infty} = 47 \pm 1 \text{ AU}, \quad (2.32)$$

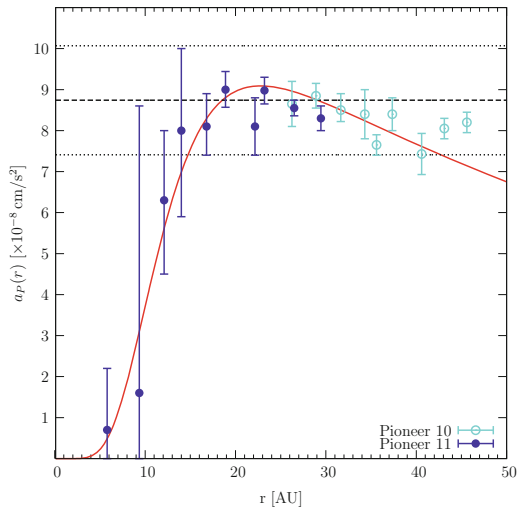
$$\bar{r} = 4.6 \pm 0.2 \text{ AU}, \quad (2.33)$$

$$b = 4.0. \quad (2.34)$$

The graph in Fig. 2.6 plots the obtained prediction for the anomalous acceleration compared with the data from both Pioneer probes.

Finally, the authors argue that the STVG theory can explain the anomalous acceleration and still be consistent with the equivalence principle, lunar laser ranging and satellite data for the inner solar system as well as the outer solar system planets [12].

Fig. 2.6 Best fit to the Pioneer anomalous acceleration data plotted against the position, r in AU, on a linear scale out to $r = 50$ AU, as presented in Ref. [12]. Compare with Fig. 2.4



2.3 Point-Like Source Method

2.3.1 Motivation

Even during the most heated part of the debate, every assessment of the anomalous acceleration left open the effect due to thermal radiation. The implication was that thermal effects became a controversial issue, which meant that a reliable estimate of these effects was key to the understanding of the problem.

The more conventional approach would be to construct a detailed finite-element model of the spacecraft and, based on individual instrument power consumptions, produce a map of external surface temperatures from which thermal radiation would be derived. This was the path followed by the teams working out the issue at ZARM [24] and the JPL [25].

The main disadvantage of these methods in this context is their reliance on a very accurate knowledge of all the engineering details involved, including structural configuration and dimensions, thermal and optical properties of the materials used and individual instrument power consumptions. Much of this information was not easily available, meaning that any effort to model Pioneer 10 and 11 through these methods would necessarily involve a significant amount of guessing. Moreover, the finite-element models are too slow to allow for the testing of a wide enough range of values for the poorly known parameters. Up until recently, there was also no unequivocal characterisation of the acceleration, implying that the efficiency of such an effort would be limited.

This problem required an approach that, not only kept the physical formulation transparent, but also combined a high degree of flexibility and computational speed.

The choice made by our team was to develop a new approach that would be able to tackle this issue with all its challenges. We called this the *point-like source method*, due to one of its key features, the modelling of the spacecraft's thermal emissions through a distribution of a small number of carefully placed point-like radiation sources.

In order to ensure that simplicity was not achieved at the expense of accuracy, a battery of test cases was performed to evaluate the robustness of the results. The outcome of these test cases, discussed in Sect. 2.3.3, validates the approach by showing that, for the typical configurations of the surfaces in the spacecraft, the result converges rapidly and with a relatively small number of point-like sources [22].

One key feature of the point-like source method is that it easily allows for the variation of parameters involving a large degree of uncertainty. This is related to the geometrical and material properties of the various spacecraft elements, which, in most cases, do not have well-known values, even at launch, and have endured extended periods of degradation in space. We have used a Monte Carlo simulation, by assigning a statistical distribution to the values of each parameter, based on the available information, and generating a large number of random values to obtain a probability distribution for the final result [23].

The fact that this method produced results that are generally in agreement with the ones obtained through subsequent, more detailed finite-element models [24, 25], is a further indication of its reliability and robustness. This was further demonstrated by its successful application to the study of the Cassini spacecraft, discussed in Chap. 3 of this thesis [26].

2.3.2 Radiative Momentum Transfer

The description of the emitted radiation, as well as its reflection, is always made in terms of the the Poynting vector, which represents the energy flux. For instance, the time-averaged Poynting vector field for a Lambertian source located at \mathbf{x}_0 is given by

$$\mathbf{S}_{\text{Lamb}}(\mathbf{x}) = \frac{W}{\pi \|\mathbf{x} - \mathbf{x}_0\|^2} \left(\mathbf{n} \cdot \frac{\mathbf{x} - \mathbf{x}_0}{\|\mathbf{x} - \mathbf{x}_0\|} \right) \frac{\mathbf{x} - \mathbf{x}_0}{\|\mathbf{x} - \mathbf{x}_0\|}, \quad (2.35)$$

for $\mathbf{n} \cdot (\mathbf{x} - \mathbf{x}_0) \geq 0$, where W is the emissive power and \mathbf{n} is the emitting surface normal.

Despite its point-like nature, the method can be easily extended to include other radiation source geometries, as long as they have a straightforward mathematical description and preserve energy conservation. An example that turned out to be especially useful in the thermal modelling of Cassini [26] is the cylindrical source, where the emitter is a line segment instead of a point and the Poynting vector field has cylindrical symmetry. For example, one can write the time averaged Poynting vector field of a cylindrical source parallel to the x -axis with coordinates (y_0, z_0) in the yz -plane as

$$\mathbf{S}_{\text{cyl}}(\mathbf{x}) = \frac{W(0, y - y_0, z - z_0)}{2\pi l((y - y_0)^2 + (z - z_0)^2)}, \quad (2.36)$$

where W is the emissive power, l is the length of the source and $\mathbf{x} = (x, y, z)$.

From the Poynting vector field, the amount of power illuminating a given surface, W_{illum} , can be obtained by computing the Poynting vector flux through that surface, given by the integral

$$W_{\text{illum}} = \int_S \mathbf{S} \cdot \mathbf{n}_{\text{illum}} dA, \quad (2.37)$$

where $\mathbf{n}_{\text{illum}}$ is the illuminated surface normal and \mathbf{S} is the Poynting vector field resulting from the sum of all relevant radiation sources.

Since electromagnetic radiation carries momentum, its emission or absorption will translate into a force being exerted on illuminated surfaces. This is usually expressed as a *radiation pressure*, P_{rad} , given, for an opaque illuminated surface by the power flux divided by the speed of light

$$P_{\text{rad}} = \frac{\mathbf{S} \cdot \mathbf{n}_{\text{illum}}}{c}. \quad (2.38)$$

In the case of a radiation source, the radiation pressure has its sign reversed relative to the direction of emission. If there is transmission (i.e., the surface is not opaque) the pressure is multiplied by the absorption coefficient. As to reflection, we shall see in Sect. 2.3.4 that it can be treated as an absorption followed by a partial re-emission of the radiation.

Integrating the radiation pressure on a surface allows us to obtain the force and, dividing by the mass of the spacecraft, m_{sc} , the acceleration due to thermal radiation

$$\mathbf{a}_{\text{th}} = \frac{1}{m_{\text{sc}}} \int_S \frac{\mathbf{S} \cdot \mathbf{n}_{\text{illum}}}{c} \frac{\mathbf{S}}{||\mathbf{S}||} dA. \quad (2.39)$$

To determine the force exerted by the radiation on the emitting surface, the integral should be taken over a closed surface encompassing the latter in order to determine the total momentum carried by the radiation. Equivalently, the force exerted by the radiation on an illuminated surface requires an integration surface that encompasses it. Furthermore, considering a set of emitting and illuminated surfaces implies the proper accounting of the effect of the shadows cast by the various surfaces, which are then subtracted from the estimated force on the emitting surface. One may then read the thermally induced acceleration directly.

It should be highlighted at this point that the formulation here presented relies solely on the power balance of the spacecraft's external surfaces and there is no intermediate step where the temperatures are obtained. This is important because it shortcuts the uncertainty related to the fragmented and incomplete data on surface emissivities and the limited onboard temperature telemetry data. As discussed further on, in Sect. 2.4.5, the data on the power supply is much more reliable.

2.3.3 Test Cases

The innovative character of this method makes it wise to conduct a series of test cases to confirm if it delivers the correct results. The purpose is to assess the quality of the results and to gain sensitivity to the errors involved in the kind of approximations that are performed. The main issue is to ascertain if the radiation emitted from an extended surface can be adequately represented by a small number of point-like sources instead of a very fine mesh of radiating elements.

The test case setup includes a 1 m^2 emitting surface and a second absorbing surface of similar size set at various distances and angles. These characteristic sizes and distances were chosen to be of the same order of magnitude as those involved in the construction of the kind of spacecraft under analysis. The radiation emissions are modelled with an increasingly finer mesh of point-like Lambertian sources and the results for the energy flux and force are then compared and analysed for convergence.

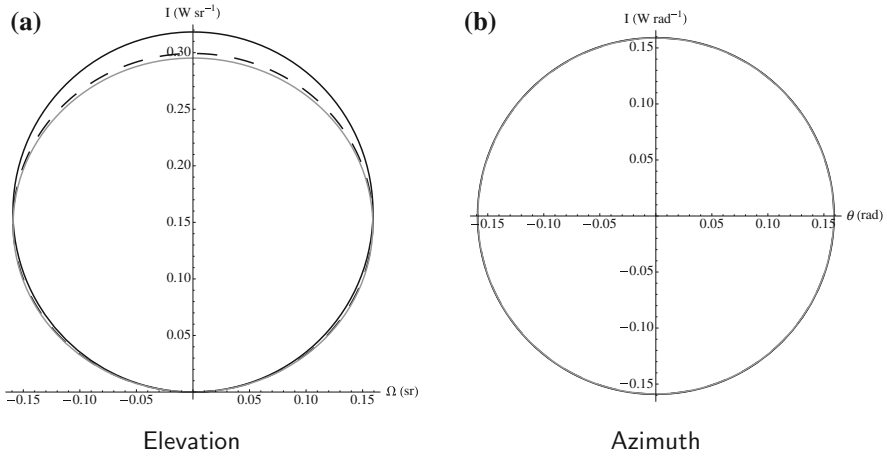


Fig. 2.7 Polar plot of the energy flux variation with elevation and azimuth of the radiation emitted by a surface on the xy -plane, when considering 1, 4 and 16 Lambertian sources (*full*, *dashed* and *grey* curves, respectively), maintaining the total emitted power constant at 1 W. The curves for 64 or 144 sources overlap the one for 16 sources). The intensity at higher elevations (close to vertical) diminishes with the number of sources, compensating the slight increase at the lower angles

For a single radiation emitting surface without any other illuminated surfaces, the force is normal to it and only depends on the total emitted power. Integrating Eq. (2.39) along a closed surface encompassing the emitting surface in the xy -plane, we obtain a force pointing in the z -axis, of magnitude $(2/3)W/c$, where W is the emitted power and c is the speed of light.

Computation of the shadow and radiation pressure on a second surface yields results that are not independent from the source distribution. In order to acquire some sensibility on that dependence, we plot the variation of the radiation intensity with the elevation and the azimuth for 1, 4, 16, 64 and 144 source meshes, as depicted in Fig. 2.7. These plots are obtained by integrating the energy flux along the azimuth or elevation.

A visual inspection of the results indicates that, even for the simpler 1 source mesh, the maximum deviation occurs at the higher angles of elevation and is less than 10 %, when compared to the 144 source mesh. Except in cases where surfaces directly face each other, deviations should be considerably smaller. One also verifies that convergence is achieved very rapidly, since the intensity plots for 16, 64 and 144 source meshes are superimposed, having minimal differences between them.

In order to confirm this intuitive perception, the force acting on a second 1 m^2 surface is computed for several different positions. A total of nine configurations were tested, with different positions and tilt angles, as listed in Table 2.3. Two of the configurations are also illustrated in Fig. 2.8 as examples. The results are then obtained for 1, 4, 16, 64 and 144 source meshes. The configurations were chosen to be representative of the typical dimensions and angles involved in the geometric

Table 2.3 Positions considered for the illuminated surface in test cases

Test case	Surface centre position (m)	Surface tilt angle (°)
1	(2, 0, 0.5)	90
2	(2, 0, 1.5)	0
3	(2, 0, 1.5)	30
4	(2, 0, 1.5)	60
5	(2, 0, 1.5)	90
6	(1, 0, 2)	0
7	(1, 0, 2)	30
8	(1, 0, 2)	60
9	(1, 0, 2)	90

The first (emitting) surface is in the xy plane centred at the origin. Considered distances between both surfaces are typical for the Pioneer spacecraft

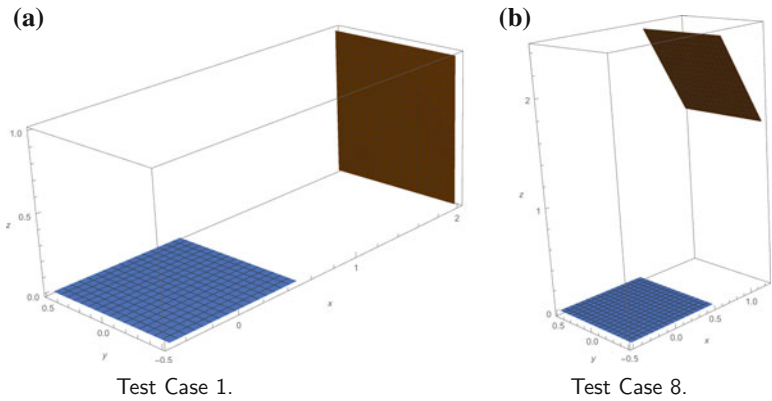


Fig. 2.8 Geometry of test cases 1 and 8 (cf. Table 2.3). Thermal emission from a surface is simulated by a different number of Lambertian sources evenly distributed on the surface, maintaining the total emitted power constant, and the effect on a second surface is observed. This is the test case where the highest variation with the number os sources considered were obtained

configurations of the kind of spacecraft in question. The full results for the energy flux and force components for each test case are presented in Appendix A.

Of all the analysed cases, the highest deviation occurs for Test Case 8, confirming previous expectations, since the second surface is set at high elevation from the emitting surface, as depicted in Fig. 2.8b. The results in Table 2.4 show a difference of approximately 6 % between the force obtained with one source and the results for the finer meshes (16, 64 and 144 sources). Nevertheless, the latter are all within 0.5 % of each other, and the intermediate 4 source mesh has a deviation of under 1.5 % to the 144 source mesh.

Table 2.4 Results for test case 8 considering a total emission of 1 kW

Sources	Energy Flux (W)	Δ (%)	Force components (x, y, z) (10^{-7} N)	Force intensity (10^{-7} N)	Δ (%)
1	45.53		(2.016, 0, 2.083)	2.899	
4	43.85	3.7	(1.918, 0, 2.003)	2.773	4.3
16	43.45	0.93	(1.895, 0, 1.984)	2.744	1.1
64	43.35	0.23	(1.890, 0, 1.979)	2.736	0.27
144	43.33	0.043	(1.889, 0, 1.978)	2.735	0.050

As the number of sources to represent the thermal emission of a surface change, the resultant force components on the secondary surface remain almost the same

Table 2.5 Same as Table 2.4, for test case 1

Sources	Energy Flux (W)	Δ (%)	Force components (x, y, z) (10^{-7} N)	Force intensity (10^{-7} N)	Δ (%)
1	15.34		(0.9300, 0, 0.1514)	1.004	
4	15.92	3.8	(1.028, 0, 0.1638)	1.041	3.6
16	16.09	1.0	(1.038, 0, 0.1675)	1.051	0.98
64	16.13	0.26	(1.040, 0, 0.1684)	1.054	0.25
144	16.14	0.049	(1.041, 0, 0.1686)	1.054	0.047

For the typical angles of the most common space probe configurations, one may take as figure of merit Test Case 1, depicted in Fig. 2.8a, with the results shown in Table 2.5. The analysis of these results shows that, for 16, 64 and 144 sources, the variation in the energy flux and force is, again less than 0.5 %. In addition to that, the difference to the finer meshes is less than 5 % for 1 source and less than 1.5 % for a 4 source mesh.

An inspection of the remaining cases listed in Appendix A yields similar conclusions. For all test cases examined, the convergence of the results occurs at a similar pace and yields similarly small deviations. These results provide a fairly good illustration of the power of the proposed method and how well we can estimate the radiation effects on the Pioneer probes and other problems with similar requirements. The deviations are always well below 10 %, even with the roughest simplifications allowed by the method. We may then conclude that, for the scales and geometry involved in a thermal model of a space probe such as the Pioneer 10 and 11, the source distribution method is, not only consistent and convergent, but that it provides a very satisfactory account of the thermal radiation effects, considering all uncertainties involved.

After analysing the convergence of the method, we also wanted to assess the effect of ignoring minor surface features, such as the equipment attached to the external walls of the spacecraft and other geometric details. For that we considered

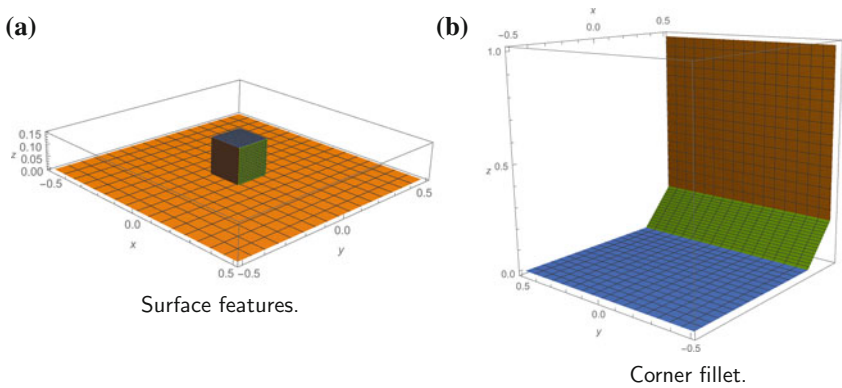


Fig. 2.9 Geometry for the surface features and corner fillet test cases. A cubical shape is placed on top of the flat surface and the force is compared for different sizes of this cube, while the total power is kept constant

Table 2.6 Results for the surface feature test case where the impact of ignoring a cubic shape placed on top of a 1 m² flat surface is analysed

Feature height (cm)	Force intensity (10 ⁻⁶ N)	Δ (%)
0	2.224	
1	2.223	0.040
5	2.202	1.0
10	2.139	3.9

The total power is kept constant at 1 kW and the temperature is assumed uniform in all surfaces. The deviations Δ with respect to the plane surface without any features are small enough to allow this simplification

two additional test cases. The particular situations analysed were a cubical piece on top of a 1 m² flat surface, as shown in Fig. 2.9a, and two perpendicular surfaces with a fillet (a “cut corner”), as in Fig. 2.9b. In each case, the force resulting from the emissions of the surfaces was compared. The total power is kept constant and the temperature is assumed uniform in all surfaces.

The results presented in Tables 2.6 and 2.7 set boundaries on the kind of geometric simplifications that can be made without a significant impact in the final result and keeping in line with the accuracy targets set for this study.

These results indicate that, in the absence of large temperature gradients, no significant errors will arise from considering flat surfaces and not taking into account all the minute details of the spacecraft.

Table 2.7 Results for the corner fillet test case with a constant total power of 1 kW

Fillet dimension (cm)	Force components (x, y, z) (10^{-7} N)	Force intensity (10^{-7} N)	Δ (%)
0	(1.112, -1.112, 0)	1.573	
1	(1.115, -1.115, 0)	1.577	0.2
5	(1.129, -1.129, 0)	1.596	1.5
10	(1.146, -1.146, 0)	1.620	3.0
20	(1.181, -1.181, 0)	1.670	6.2

The deviation Δ of the force intensity with respect to the sharp corner are kept within reasonable values

2.3.4 Reflection Modelling: Phong Shading

The inclusion of reflections in the model is achieved through a method known as *Phong Shading*, a set of techniques and algorithms commonly used to render the illumination of surfaces in three-dimensional computer graphics [27].

This methodology includes a reflection model which accounts for diffusive and specular reflection, known as *Phong reflection model*, and an interpolation method for curved surfaces modelled as polygons, known as *Phong interpolation*.

The Phong reflection model is based on an empirical formula that gives the illumination value of a given point in a surface, I_p , as

$$I_p = k_a i_a + \sum_{m \in \text{lights}} [k_d (\mathbf{l}_m \cdot \mathbf{n}) i_d + k_s (\mathbf{r}_m \cdot \mathbf{v})^\alpha i_s], \quad (2.40)$$

where k_a , k_d and k_s are the ambient, diffusive and specular reflection constants, i_a , i_d and i_s are the respective light source intensities, \mathbf{l}_m is the direction of the light source m , \mathbf{n} is the surface normal, \mathbf{r}_m is the direction of the reflected ray, \mathbf{v} is the direction of the observer and α is a “shininess” constant (the higher it is, the more mirror-like is the surface).

In using this formulation to solve a physics problem, there are a few constraints that should be taken into account. The ambient light parameter k_a and i_a , while useful in computer graphics, are not relevant for this problem since they give the reflection behavior relative to a background radiation source. Also, the intensities i_d and i_s should be the same, since the diffusive and specular reflection are relative to the same radiation sources.

This method provides a simple and straightforward way to model the various components of reflection, as well as an accurate accounting of the thermal radiation exchanges between the surfaces on the spacecraft. In principle, there is no difference between the treatment of thermal infrared radiation and visible light, for which the method was originally devised, allowing for a natural wavelength dependence of the above material constants.

Bearing in mind the formulation used in Sect. 2.3.2, the Phong shading methodology must be adapted from a formulation based on intensities (energy per unit surface of the projected emitting surface) to one based on the energy-flux per unit surface (the Poynting vector). This led to two expressions for the diffusive and specular components of reflection in terms of the Poynting vector field. Thus, the diffusively reflected radiation Poynting vector field is given by

$$\mathbf{S}_{\text{rd}}(\mathbf{x}, \mathbf{x}') = \frac{k_d |\mathbf{S}(\mathbf{x}') \cdot \mathbf{n}|}{\pi \|\mathbf{x} - \mathbf{x}'\|^2} \mathbf{n} \cdot (\mathbf{x} - \mathbf{x}') \frac{\mathbf{x} - \mathbf{x}'}{\|\mathbf{x} - \mathbf{x}'\|}, \quad (2.41)$$

while the specular component reads

$$\mathbf{S}_{\text{rs}}(\mathbf{x}, \mathbf{x}') = \frac{k_s |\mathbf{S}(\mathbf{x}') \cdot \mathbf{n}|}{\frac{2\pi}{1+\alpha} \|\mathbf{x} - \mathbf{x}'\|^2} [\mathbf{r} \cdot (\mathbf{x} - \mathbf{x}')]^\alpha \frac{\mathbf{x} - \mathbf{x}'}{\|\mathbf{x} - \mathbf{x}'\|}, \quad (2.42)$$

where \mathbf{x}' is a point on the reflecting surface. In both cases, the reflected radiation field depends on the incident radiation field $\mathbf{S}(\mathbf{x}')$ and on the reflection coefficients k_d and k_s , respectively.

Using Eqs. (2.41) and (2.42), one can now compute the reflected radiation field by adding up both components. From the emitted and reflected radiation vector fields, the irradiation of each surface is then computed and, from that, the contribution to the acceleration can be obtained through Eq. (2.39).

To summarise, the first step in the procedure is, once the radiation source distribution is put in place, to compute the emitted radiation field and the respective force exerted on the emitting surfaces. This is followed by the determination of which surfaces are illuminated and the computation of the force exerted on those surfaces by the radiation. At this stage, we get a figure for the thermal force without reflections. The reflection radiation field is then computed for each surface and subject to the same steps as the initially emitted radiation field, leading to a determination of thermal force with one reflection.

This method can, in principle, be iteratively extended to as many reflection steps as desired, considering the numerical integration algorithms and available computational power. If necessary, the computation time in each step can be reduced through a discretisation of the reflecting surface into point-like reflectors.

2.4 Pioneer Thermal Model

2.4.1 Geometric Model

The construction of a geometric model of the Pioneer space probes that follows the principles outlined in the previous section is the first task to perform in the study of Pioneer 10 and 11 thermal effects.

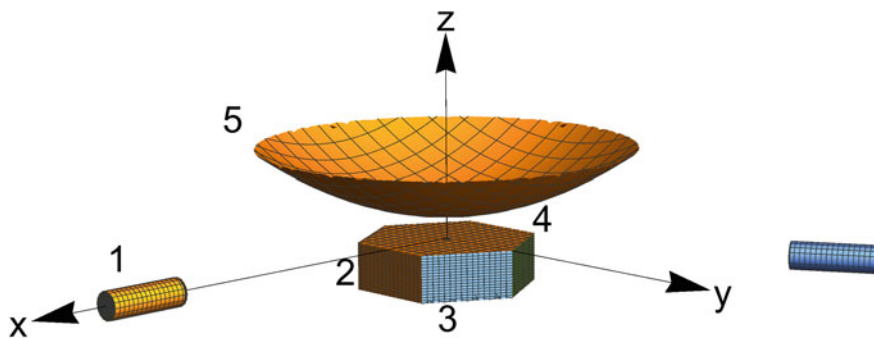


Fig. 2.10 Three-dimensional simplified geometric model of Pioneer 10 and 11 showing the configuration of the RTGs (1), the main equipment compartment with its side (2), front (3) and back walls (4), and the parabolic high-gain antenna (5)

The geometric model used in this study retains the most important features of the Pioneer spacecraft, namely:

- (i) the parabolic high-gain antenna,
- (ii) the main equipment compartment behind the antenna,
- (iii) two Radioisotope Thermal Generators (RTGs), cylindrical in shape, each connected to the main compartment through a truss.

The full shape of the geometric model is depicted in Fig. 2.10 as a three-dimensional image, labeled with the reference system used, and in Fig. 2.11 as a drawing with dimensions.

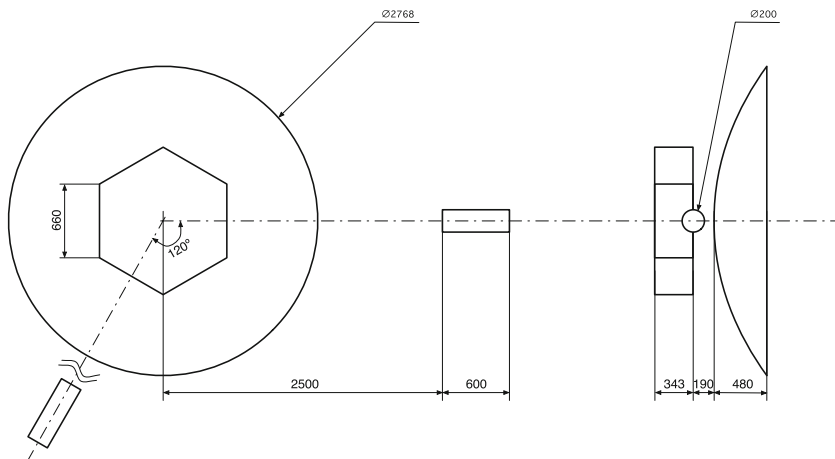


Fig. 2.11 Schematics of the Pioneer geometric model used in this study, with relevant dimensions (in mm); second RTG truss is not represented to scale. Lateral view indicates the relative position of the RTGs, box compartment and the gap between the latter and the high-gain antenna

This model simplifies the surface features and minor details of the spacecraft. This approximation has been tested through specific test-cases (*cf.* Sect. 2.3.3) which show that the effect on the final result is under 5 % and can be safely ignored for the purposes of this study.

2.4.2 Order of Magnitude Analysis

Before undertaking a more rigorous numerical computation, it is useful to perform a preliminary order of magnitude analysis. This allows one to obtain a concrete figure of merit for the overall acceleration arising from thermal effects, which can be compared with the $a_{\text{Pioneer}} \sim 10^{-9} \text{ m/s}^2$ scale of the Pioneer anomaly.

From the spacecraft specifications, one has a total mass $m_{\text{Pioneer}} \sim 230 \text{ kg}$, and separate RTG and equipment compartment powers $W_{\text{RTG}} \sim 2 \text{ kW}$ and $W_{\text{equip}} \sim 100 \text{ W}$, respectively. As already discussed, the integration of the emissions of the RTG and instrument compartment indicate the proportion of emitted power that is effectively converted into thrust. If we assume uniform temperature and emissivity in the RTGs and equipment compartment, we obtain

$$\begin{aligned} F_{\text{RTG}} &\sim 2 \times 10^{-2} \frac{W_{\text{RTG}}}{c}, \\ F_{\text{sides}} &\sim 10^{-1} \frac{W_{\text{equip}}}{c}, \\ F_{\text{front}} &\sim 2 \times 10^{-1} \frac{W_{\text{equip}}}{c}, \end{aligned} \tag{2.43}$$

where F_{RTG} , F_{sides} and F_{front} denote the contributions from the RTG, equipment side walls and front wall, respectively, and c is the speed of light.

Dividing by the mass, one can easily estimate the acceleration of the spacecraft due to the thermal effects arising from the power dissipation of the RTGs and equipment compartment

$$\begin{aligned} a_{\text{RTG}} &\sim 2 \times 10^{-2} \frac{W_{\text{RTG}}}{m_{\text{Pioneer}} c} \sim 6 \times 10^{-10} \text{ m/s}^2, \\ a_{\text{equip}} &\sim 3 \times 10^{-1} \frac{W_{\text{equip}}}{m_{\text{Pioneer}} c} \sim 4.4 \times 10^{-10} \text{ m/s}^2. \end{aligned} \tag{2.44}$$

This clearly indicates that both contributions are relevant to account for the reported anomalous acceleration. Furthermore, it also shows that the RTGs and the instrument compartment yield thermal effects of similar magnitudes, so that one cannot focus solely on one of these sources when modelling the spacecraft. This had already been revealed by the analysis in Ref. [28].

2.4.3 Heat Conduction

Aside from radiative heat transfer, some conduction is expected between the structurally connected components of the spacecraft, thus affecting the distribution of radiated energy. Naturally, this will tend to warm the colder elements and cool the hotter ones, until a new equilibrium situation is achieved (more rigorously, a quasi-equilibrium, since the timescale of radiation and conduction is much smaller than that of the decreasing overall power output).

Thus, one should inspect the impact of this heat transfer in the main structural elements, namely between the RTGs and the main compartment and the main compartment and the high gain antenna. Conduction is expected to be larger between the RTGs and the main compartment: assuming that the latter is at about 0°C (a worst case scenario, as it is warmed by the electronics to $\sim 10^\circ\text{C}$), while the RTGs are at $\sim 150^\circ\text{C}$, a temperature gradient of approximately 60 K/m is obtained. The total cross-section of the three small diameter rods composing each truss is estimated to be of the order of 10^{-4} m^2 ; these are made of aluminium, with a conductivity of approximately 240 W/(m K) . Using these figures, a total conducted power of the order of 1 W (up to 4 W in more conservative estimates) is obtained [22].

This is two orders of magnitude below the power of the main compartment and three orders of magnitude below the RTG power and can therefore be neglected. Since the temperature gradient between the main compartment to the antenna is much smaller than the one considered above, the related heat conduction is well below 1 W . Thus, one may safely disregard the contribution arising from conduction when computing the distribution of heat radiation.

2.4.4 Thermal Radiation Model

To begin the discussion surrounding the building of the thermal radiation model, it is important to highlight that this task is considerably simplified by the fact that the Pioneer probes are spin-stabilised. This implies that the effect of all emissions normal to the z axis are cancelled out after each complete revolution of the spacecraft, leaving only the contribution along the antenna's axis.

Using the point-like source method, we can now compute the contribution of the individual components listed in Table 2.8. This is achieved by integrating Eq. (2.39) in three successive steps. First, the emitted radiation field given by Eq. (2.35) is integrated along a closed surface, yielding the first-order effect due to the emissions. Afterwards, the same radiation field is integrated along the illuminated surfaces, in order to subtract the shadow effect. Finally, the reflected radiation vector-field, given by Eqs. (2.41) and (2.42), is integrated along closed surfaces, adding the contribution from reflection.

This process allows us to obtain the values for the force in terms of the emitted powers and reflection coefficients. As pointed out before, the results that follow

Table 2.8 Labelling of the considered contribution to the Pioneer 10 and 11 thermal acceleration

Emitting surface	Reflecting surface	Label
RTG	Side of main compartment	F_{12}
RTG	High-gain antenna dish	F_{15}
Side of main compartment	High-gain antenna dish	F_{25}
Front of main compartment	None	F_3
Back of main compartment	High-gain antenna dish	F_{45}

are only presented along the axis of the main antenna, since all radial components cancel-out. A positive figure indicates a sunward force.

The two main contributors to thermal emissions aboard Pioneer 10 and 11 are the RTGs, where the main power source of the spacecraft is located, and the main equipment compartment, where most of the generated electrical power is consumed. Emissions from the RTGs illuminate both the high-gain antenna and the lateral walls of the main equipment compartment. Radiation originating in the main compartment only significantly illuminates the main antenna, since the RTGs are too small and distant to yield any significant contribution from absorption or reflection.

The relevant contributions for this analysis are summarised in Table 2.8, with the labels used throughout the rest of this section. The complete set of radiation sources used in the model is listed in Table 2.9 and are described in the following paragraphs.

Table 2.9 Position and direction of the Lambertian sources used to model each emitting surface of the Pioneer spacecraft model

Emitting surface	Source	Position (m)	Surface normal (m)
Front wall (index 4)	1	(0, 0, -0.343)	(0, 0, -1)
Lateral wall (only one modelled)	1	(0.572, 0.2475, -0.172)	(1, 0, 0)
	2	(0.572, 0.0825, -0.172)	(1, 0, 0)
	3	(0.572, -0.0825, -0.172)	(1, 0, 0)
	4	(0.572, -0.2475, -0.172)	(1, 0, 0)
RTG (only one modelled)	1	(2.5, 0, 0)	(-1, 0, 0)
	2	(3.1, 0, 0)	(1, 0, 0)
Back wall	1	(0.381, 0, 0)	(0, 0, 1)
	2	(0.191, 0.33, 0)	(0, 0, 1)
	3	(-0.193, 0, 33)	(0, 0, 1)
	4	(-0.381, 0, 0)	(0, 0, 1)
	5	(-0.191, -0.33, 0)	(0, 0, 1)
	6	(0.191, -0.33, 0)	(0, 0, 1)

The front wall of the main equipment compartment (facing away from the sun and equipped with the heat-dissipating louvers) emits radiation directly into space, not illuminating any other surface. Furthermore, this surface is orthogonal to the spacecraft's spin axis. It can then be modelled by simply resorting to a single radiation source, without any impact on the accuracy of the final result.

The emitted radiation field is obtained by replacing the position of the radiation source and surface normal direction in Eq. (2.35). The force exerted by the radiation field on the emitting surface is obtained by integrating Eq. (2.39) along a closed surface. The resulting force exerted by the emitted radiation on the surface along the z axis is, as expected, given by

$$F_3 = \frac{2}{3} \frac{W_{\text{front}}}{c}, \quad (2.45)$$

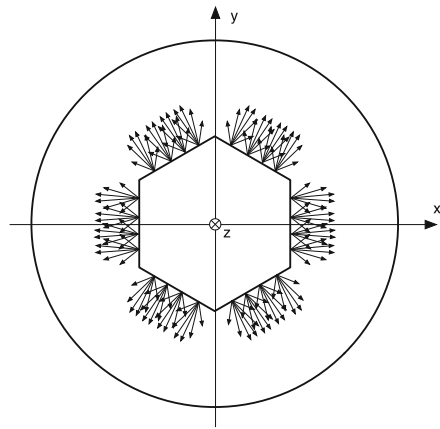
where W_{front} is the emitted power.

The side walls of this compartment are each modelled by four Lambertian sources, as depicted in Fig. 2.12. The test cases and a previously performed convergence analysis showed that this is sufficient to reach the necessary accuracy [21, 22].

The radiation coming from the lateral walls of the main equipment compartment illuminates the high-gain antenna. Due to the symmetry of the problem, and neglecting the interaction with the small far RTGs, it is only necessary to model one of the six walls. The set of Lambertian sources used for one of these walls is indicated in Table 2.9. The z component of the radiation field force on the emitting surface vanishes, as the emitting surface is perpendicular to the z -axis.

Using Eq. (2.39), but taking the integral over the illuminated portion of the antenna dish, we obtain the force exerted on the illuminated surface, which accounts for the shadow effect. This gives a z component of $-0.0738(W_{\text{sides}}/c)$, where W_{sides} is the power emitted from the lateral walls, to be subtracted from the total force of the emitted radiation.

Fig. 2.12 Schematics of the configuration of Lambertian sources used to model the lateral walls of Pioneer's main equipment compartment



In what concerns the computation of diffusive reflection, Eq. (2.41) allows for the computation of the reflected Poynting vector-field $\mathbf{S}_{rd}(\mathbf{x}, \mathbf{x}')$ due to the emitted radiation field $\mathbf{S}(\mathbf{x}')$, where \mathbf{x}' is a point in the reflecting surface. The reflected radiation field is given for each point in the reflecting surface. Consequently, it must be integrated first over the reflecting surface, conveniently parameterised, giving the resulting reflected radiation field, and then through Eq. (2.39) over a closed surface, in order to compute the force resulting from the reflected radiation. The procedure for specular reflection is analogous, except that Eq. (2.42) should instead be used to obtain the reflected radiation field.

Integrating the vector field representing radiation from the lateral walls of the main compartment reflecting on the high-gain antenna, we obtain a force result of $0.0537k_{d,ant}(W_{sides}/c)$ for the diffusive component and $0.0089k_{s,ant}(W_{sides}/c)$ for the specular component, where $k_{d,ant}$ and $k_{s,ant}$ are the diffusive and specular reflection coefficients of the main antenna, respectively.

The result for this contribution is given by adding the emitted radiation force (zero), the shadow effect and both components of reflection, leading to

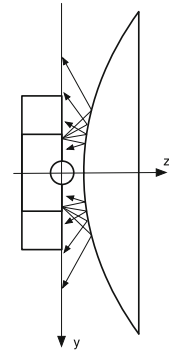
$$F_{25} = \frac{W_{sides}}{c} (0.0738 + 0.0537k_{d,ant} + 0.0089k_{s,ant}), \quad (2.46)$$

where W_{sides} is the power emitted by the lateral walls of the main compartment, and $k_{d,ant}$ and $k_{s,ant}$ are the diffusive and specular reflection coefficients of the main antenna, respectively.

The back wall of the main equipment compartment faces the back of high-gain antenna. The radiation from this wall will, at a first iteration, reflect off the antenna and add a contribution to the force in the direction of the sun, as depicted in Fig. 2.13. This back wall was modelled using a set of six Lambertian sources evenly distributed in the hexagonal shape.

Initially, it was expected that the contribution from radiation emitted from the back wall of the main compartment and reflecting in the space between this compartment and the antenna dish would be small.

Fig. 2.13 Schematics of the configuration of Lambertian sources used to model the back wall of the main equipment compartment and the first reflection on the main antenna dish



In order to verify this assumption, a computation was made using the method described above. The results ultimately show that this contribution cannot be discarded after all, as it may be relevant in the final result. Considering one reflection from the antenna dish, the result in terms of the emitted power from the back wall of the main compartment W_{back} , by

$$F_{45} = \frac{W_{\text{back}}}{c} \left(-\frac{2}{3} + 0.5872 + 0.5040k_{\text{d,ant}} + 0.3479k_{\text{s,ant}} \right). \quad (2.47)$$

In the preceding equation, $-\frac{2}{3} \frac{W_{\text{back}}}{c}$ is the contribution from the emitted radiation and $0.5872 \frac{W_{\text{back}}}{c}$ is the effect of the antenna's shadow. The remaining terms are the reflective contributions.

Finally, the RTGs can be easily and effectively modelled by two Lambertian sources, one at each base of the cylinder, as shown in Fig. 2.14. The emissions from the lateral walls need not to be considered since the radiation field has cylindrical symmetry and does not illuminate any surface. Also, radiation from the outward facing base radiates directly into space in a radial direction and its time averaged contribution is null. This leaves only the radiation emitted towards the centre of the spacecraft, that is reflected by both the high-gain antenna and the main equipment compartment.

Only one RTG needs to be modelled, since the effect of the components normal to the z axis will be cancelled-out at each revolution of the spacecraft.

Using the same procedure, the force generated by the RTG emissions is thus given in terms of the power emitted from the RTG bases facing the centre of the spacecraft W_{RTGb} . The force resulting from reflections on the antenna is given by

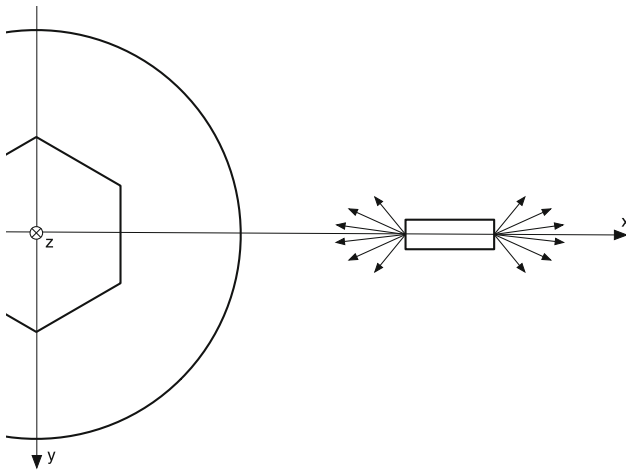


Fig. 2.14 Schematics of the two Lambertian sources used to model each RTG

$$F_{15} = \frac{W_{\text{RTGb}}}{c} (0.0283 + 0.0478k_{\text{d,ant}} + 0.0502k_{\text{s,ant}}), \quad (2.48)$$

and the contribution from reflections on the lateral surfaces of the main equipment compartment is

$$F_{12} = \frac{W_{\text{RTGb}}}{c} (-0.0016 + 0.0013k_{\text{s,sides}}), \quad (2.49)$$

where $k_{\text{d,ant}}$, $k_{\text{s,ant}}$, $k_{\text{d,sides}}$ and $k_{\text{s,sides}}$ are the respective reflection coefficients.

These force computations allow for obtaining, once the respective powers and reflection coefficients are inserted, of the acceleration due to thermal dissipation mechanisms is given by

$$a_{\text{Pioneer}} = \frac{F_{12} + F_{15} + F_{25} + F_3 + F_{45}}{m_{\text{Pioneer}}}, \quad (2.50)$$

where the spacecraft's mass is taken to be approximately $m_{\text{Pioneer}} = 230$ kg. This figure considers a total launch mass of 259 kg, including 36 kg of hydrazine propellant that was partially consumed in the early stages of the mission [5]. Note that this is an approximate figure, since the actual masses for the Pioneer 10 and 11 would be slightly different due to different fuel consumptions along their respective missions.

2.4.5 Power Supply

The available onboard power was chosen as the independent variable in the computation of the thermally induced acceleration. This choice is justified with the fact that the available power is reasonably well known. Indeed, it is one of the few parameters with consistent data available throughout the operational life of the probes.

All the power on board the Pioneer probes comes from the two plutonium RTGs. It is thus easy to compute the total power available, considering the 87.74 year half-life of plutonium-238. According to Ref. [5], the total thermal power of the RTGs at launch was 2580 W. Consequently, its evolution with time should be given by

$$W_{\text{tot}} = 2580 \exp\left(-\frac{t \ln 2}{87.72}\right) \text{ W}, \quad (2.51)$$

with t being the time in years after launch.

The electrical power is generated by a set of thermocouples located in the RTGs. Most of this power is consumed by the various systems located in the main equipment compartment, except for a small fraction used by the radio signal. Knowing the electrical power consumption, the remaining unused power is mostly dissipated at the RTGs themselves, through suitably designed radiating fins. Thus, it is reasonable to assume that the total available power is divided into electrical power used

in equipment located in the main compartment and the remaining thermal power dissipated at the RTGs.

A good measurement of the electrical power is available through telemetry data. At launch, 120 W of electrical power were being used in the main equipment compartment plus around 20 W for the radio transmission to Earth, leaving 2420 W of thermal power in the RTGs. It is also known from telemetry data that the electrical power decayed at a faster rate than thermal power, with its half-life being around 24 years [28]. This would lead to an approximate time evolution of the electrical power in the equipment compartment given by

$$W_{\text{equip}} \approx 120 \exp\left(-\frac{t \ln 2}{24}\right) \text{ W}. \quad (2.52)$$

The baseline scenarios established in the following section bear the above considerations in mind and accounts for the power values extracted from the available telemetry data for the latest stages of the mission. Specifically, the reading for the $t = 26$ years after launch. In a second stage of this study, the time evolution is taken into account, according to the reasoning developed in this section.

2.5 Results and Discussion

2.5.1 Baseline Results

In this section, a set of five scenarios is considered, while keeping the total power as $W_{\text{tot}} = 2100$ W and the electrical power as $W_{\text{equip}} = 56$ W, leaving RTG thermal power at $W_{\text{RTG}} = 2024$ W (assuming the power of the radio beam is still 20 W).

The simplest possibility to consider is that each component of the spacecraft has a uniform temperature. In this case, the thermal power distribution is $W_{\text{front}} = W_{\text{back}} = 17.50$ W, $W_{\text{lat}} = 21.00$ W and $W_{\text{RTGb}} = 143.86$ W, leading to a thermally induced acceleration of

$$a_{\text{th, Sc1}} = 2.27 \times 10^{-10} \text{ m/s}^2. \quad (2.53)$$

The second scenario assumes that the front wall, which is equipped with the louvers, is responsible for $W_{\text{front}} = 40$ W (that is, 70 % of 56 W) of emission, maintaining the remaining walls with uniform emission. This scenario is motivated by the essential feature of the louvers being located in the front wall of the main equipment compartment. They were designed to act as a temperature controlling element, closing or opening through the action of a bi-metallic spring. Still, even when closed, the louvers are not covered by the Multi-Layer Insulation (MLI) which shields the equipment compartment. It is then reasonable to assume that, regardless of their position, the louvers radiate a large share of the equipment power. A similar argument is presented in Ref. [10]. This leaves the lateral walls with $W_{\text{sides}} = 8.73$ W

and the back wall with $W_{\text{back}} = 7.27 \text{ W}$. The thermally induced acceleration in these conditions is

$$a_{\text{th,Sc2}} = 4.43 \times 10^{-10} \text{ m/s}^2. \quad (2.54)$$

In Scenario 3, one includes the contribution from reflections. The simplest way to achieve this is to include only the diffusive component. We consider a diffusive reflection coefficient of $k_{\text{d,ant}} = 0.8$, which would be a typical value for aluminium, used in the antenna dish. This yields a result for the acceleration of

$$a_{\text{th,Sc3}} = 5.71 \times 10^{-10} \text{ m/s}^2. \quad (2.55)$$

Scenario 4 is a variation that considers the fact that illuminated surface of the high-gain antenna is made of bare aluminium. This will make reflection from it mainly diffusive, but with a small specular highlight, as is typical of any unpolished flat metallic surface. We thus consider a reflection from the antenna dish that maintains a total reflection coefficient of 80 %, but divided in diffusive and specular components, respectively, $k_{\text{d,ant}} = 0.6$ and $k_{\text{s,ant}} = 0.2$. Furthermore, we assume a specular reflection from the MLI covering the main equipment compartment of $k_{\text{s,sides}} = 0.4$. The result from this scenario is not significantly different from Scenario 3, yielding

$$a_{\text{th,Sc4}} = 5.69 \times 10^{-10} \text{ m/s}^2. \quad (2.56)$$

In Scenario 5, in order to obtain an upper bound for the static baseline, one assumes that all the emissions of the main equipment compartment come from the louvers and a 10 % higher power from the RTG base, that is, $W_{\text{front}} = 56 \text{ W}$, $W_{\text{back}} = W_{\text{sides}} = 0 \text{ W}$ and $W_{\text{RTGb}} = 158.24 \text{ W}$. Maintaining $k_{\text{d,ant}} = 0.8$, as in Scenario 3, the upper bound for the thermal acceleration in the late stage of the mission is bound to be

$$a_{\text{th,Sc5}} = 6.71 \times 10^{-10} \text{ m/s}^2. \quad (2.57)$$

The hypotheses and results of all the analysed scenarios are summarised in Tables 2.10 and 2.11.

Table 2.10 Summary of the scenarios used to obtain baseline results for the Pioneer 10 and 11 thermal analysis

Scenario	Description
1	Uniform temperature, no reflection
2	Extra heat from louvers, no reflection
3	Scenario 2 with diffusive reflection
4	Scenario 2 with diffusive and specular reflection
5	Upper bound on all contributions

Table 2.11 Summary of results from baseline scenarios for the Pioneer 10 and 11 thermal analysis

Scenario	W_{RTGb} (W)	W_{front} (W)	W_{sides} (W)	W_{back} (W)	$k_{\text{d,ant}}$	$k_{\text{s,ant}}$	$k_{\text{s,sides}}$	a_{Pioneer} (10^{-10} m/s^2)
1	143.86	17.5	21	17.5	0	0	0	2.27
2	143.86	40	8.73	7.27	0	0	0	4.43
3	143.86	40	8.73	7.27	0.8	0	0	5.71
4	143.86	40	8.73	7.27	0.6	0.2	0.4	5.69
5	158.24	56	0	0	0.8	0	0.4	6.71

W_{lb} is the power emitted from the base of the two RTGs; W_{front} , W_{lat} and W_{back} are, respectively, the emitted powers from the front, lateral and back walls of the main equipment compartment; $k_{\text{d,ant}}$ and $k_{\text{s,ant}}$ are the diffusive and specular reflection coefficients of the high-gain antenna back; $k_{\text{s,sides}}$ is the diffusive reflection coefficient of the lateral wall of the main equipment compartment, and a_{Pioneer} is the resulting thermal acceleration along the rotation axis of the probe

With these baseline scenarios, we proceed with a static parametric analysis of the involved parameters in order to obtain a result and an error bar for the these static figures.

2.5.2 Parametric Analysis

As outlined above, the next step is to perform a static parametric analysis aiming to establish an estimate for the thermal acceleration at an instant 26 years after launch. The analysis is performed using a classic Monte-Carlo method, where a probability distribution is assigned to each variable and random values are then generated. A distribution of the final result (i.e. the acceleration) is then obtained.

The parameters that come into play in this setup are the power emitted from each surface, W_{RTGb} , W_{front} , W_{sides} , W_{back} , and the reflection coefficients $k_{\text{d,ant}}$, $k_{\text{s,ant}}$ and $k_{\text{s,lat}}$. The assertions made in the previous section regarding total power and its distribution between the RTGs and the equipment compartment remain valid.

A quick analysis of Table 2.11 allows us to draw some qualitative conclusions. For example, the amount of power emitted from the front wall W_{front} has a decisive influence in the final result. In contrast, the relevance of the specular reflection coefficient of the lateral wall $k_{\text{s,lat}}$ is almost negligible.

For the static analysis at $t = 26$ years, Scenario 4 is taken as a reference, since it is the one more solidly based on physical arguments.

The power emitted by the RTG bases facing the main compartment W_{RTGb} is generated from a normal distribution with the mean value of 143.86 W and a standard deviation of 25 % of this value. This allows for significantly larger deviation than the considered in the top-bound scenario (Scenario 5), which had only a 10 % increase in the power of this surface. The purpose is to account for unanticipated anisotropies in the temperature distribution of the RTGs.

In the case of the main equipment compartment, the focus is on the power emitted by the louvers located in the front wall. The selected distribution for the parameter W_{front} is also normal, with the mean value at 40 W (also corresponding to Scenario 4). We set the standard deviation at 7.5 W, so that the 95 % probability interval (2σ) for the value of W_{front} is below the top figure of 56 W, which corresponds to the totality of the equipment power being dissipated in the front wall. For the remaining surfaces of the equipment compartment, the power is computed at each instance so that the total power of the equipment is kept at 56 W.

Concerning the reflection coefficients for the antenna, we use uniform distributions in the intervals $[0.6, 0.8]$ for $k_{d,\text{ant}}$ and $[0, 0.2]$ for $k_{s,\text{ant}}$, while imposing the condition $k_{d,\text{ant}} + k_{s,\text{ant}} = 0.8$, since this is a typical value for aluminium in infrared wavelengths. We also expect the specular component to be small, since the surface is not polished. Furthermore, if we allow for the possibility of surface degradation with time during the mission, the specular component would suffer a progressive reduction in favour of the diffusive component, a possibility that this analysis takes into account.

We performed 10^4 Monte Carlo iterations, which easily ensures the convergence of the result. The thermal acceleration estimate yielded by the simulation for an instant 26 years after launch, with a 95 % probability level (2σ), is

$$a_{\text{th}}(26) = (5.8 \pm 1.3) \times 10^{-10} \text{ m/s}^2. \quad (2.58)$$

This result is extracted from the approximately normal distribution shown in Fig. 2.15. The conformity of the results to a normal distribution was confirmed by a Shapiro-Wilk normalcy test, and can also be qualitatively evaluated in the graph.

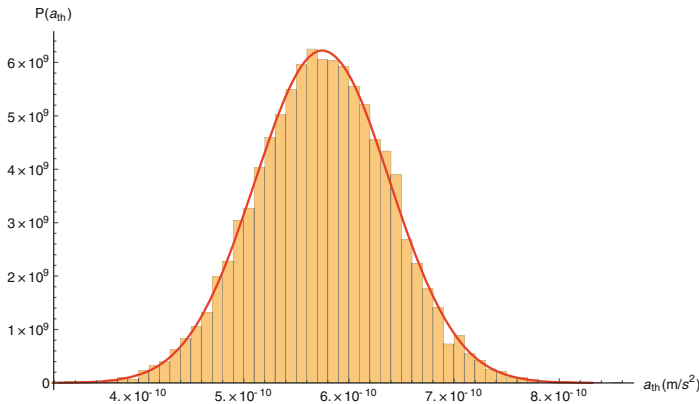


Fig. 2.15 Histogram for the probability density distribution resulting from the Monte Carlo simulation with 10,000 iterations for the thermal acceleration of the spacecraft at $t = 26$ years after launch. A Normal distribution with the same mean value and standard deviation is superimposed

These results account for between 44 and 96 % of the initially reported value $a_{\text{Pio}} = (8.74 \pm 1.33) \times 10^{-10} \text{ m/s}^2$, which, we recall, was obtained under the hypothesis of a constant acceleration. This alone, already gives a strong indication of the preponderant contribution of thermal effects to the Pioneer anomaly. However, we must proceed to obtain a time signature that can be compared with the more recent studies of the anomaly [20].

2.5.3 Time Evolution

Since thermal effects depend on the radioactive decay of the plutonium and the electrical power produced, they change with time. The final step is thus to perform an analysis of the expected time evolution of the thermal acceleration affecting the Pioneer 10 and 11 spacecraft.

An immediate estimate can be obtained by extrapolating the static results with the available time evolution of electric power, using Eqs. (2.51) and (2.52). This extrapolation, however, does not account for the possibility that some parameters may change with time, namely, the power distribution throughout the different surfaces or their reflection coefficients. This could be accounted by a simulation of the full span of the missions (i.e. a large number of consecutive simulations), with a specific prescription for the variability of these parameters.

Such task would prove too lengthy, and no significant physical insight would be gained. Hence, we have preferred a somewhat simpler approach: for a better grasp of the possibility discussed above, we apply the Monte-Carlo static analysis to only two earlier moments of the mission. Each simulation produces a central value, with top and lower bounds; these are then fitted to an exponential trend, thus obtaining an estimate of the time evolution of the thermally induced acceleration.

The selected instant for the earliest static analysis was at $t = 8$ years after launch, corresponding to the 1980 values for the Pioneer 10. This corresponds to the time at which the effect of the solar radiation pressure dropped below $5 \times 10^{-10} \text{ m/s}^2$ [5].

This analysis is made in a similar fashion as the one presented in the previous section, but using the 1980 available power values as a base for the choice of the distributions. The thermal acceleration is, in this case,

$$a_{\text{th}}(8) = (8.9 \pm 2) \times 10^{-10} \text{ m/s}^2, \quad (2.59)$$

corresponding to the same 95 % probability level in the approximately normal distribution in Fig. 2.16.

The values obtained here for this earlier stage of the mission bear a close match to those of the assumed constant anomalous acceleration.

The third static analysis was performed at a time $t = 17$ years, halfway between the other two. The estimate in this case is, for a 95 % probability,

$$a_{\text{th}}(t = 17) = (7.1 \pm 1.6) \times 10^{-10} \text{ m/s}^2. \quad (2.60)$$

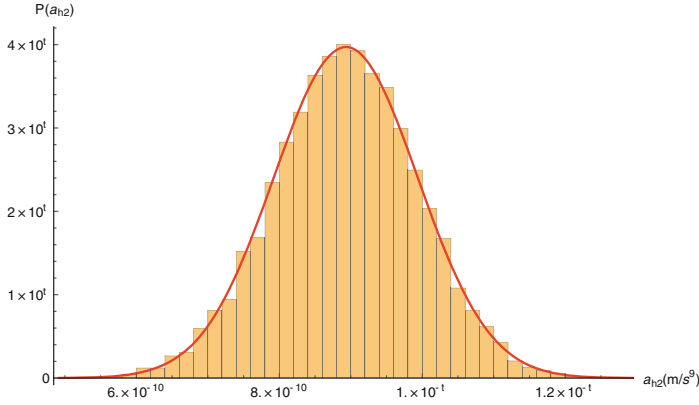


Fig. 2.16 Histogram for the probability density distribution resulting from the Monte Carlo simulation with 10,000 iterations for the thermal acceleration of the spacecraft at $t = 8$ years after launch. A Normal distribution with the same mean value and standard deviation is superimposed

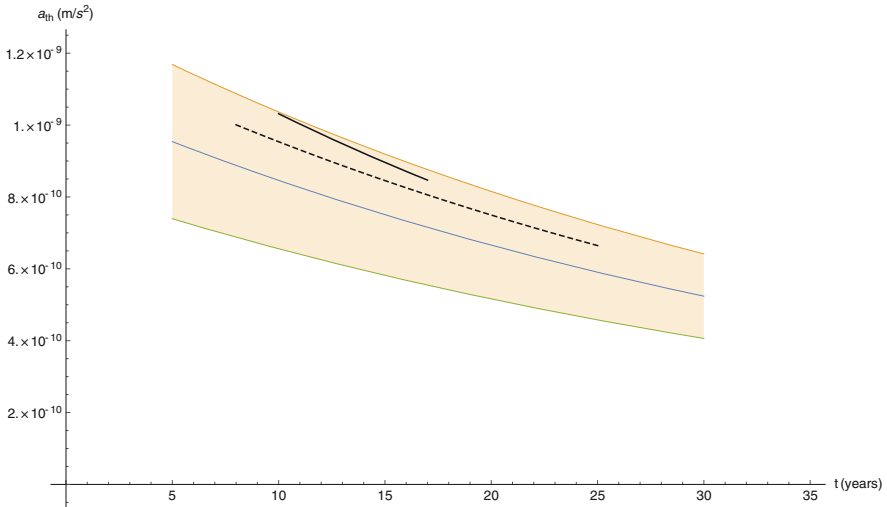


Fig. 2.17 Results for the time evolution of the thermal acceleration on the Pioneer spacecraft compared with results based on the latest data analysis of the anomalous acceleration. The *shaded area* correspond to a 95 % probability for the thermal acceleration in the time evolution analysis. For comparison, the *black dashed* and *solid lines* are based on results from the data analysis in Ref. [20]

Using the three static estimates presented above, it is now possible to produce a time evolution based on a fit to an exponential decay. This is performed for the mean value, top-bound and lower-bound of the acceleration, always based on a 2σ interval.

The curve fit for the mean, upper and lower values of the thermal acceleration reads

$$a_{\text{th}} = [(1.07 \pm 0.24) \times 10^{-9}]e^{-0.0240t} \text{ m/s}^2, \quad (2.61)$$

with t giving the time after launch in years. The time constant was averaged between the three fits, although they are all within 1 % of each other.

The time evolution resulting from any of these scenarios corresponds to a decay with a half-life of approximately 29 years, related to the nuclear decay of the plutonium in the RTGs and the faster decay rate of the electrical power, already discussed in Sect. 2.4.5. The graphic representation of the band of values predicted by our model is shown in Fig. 2.17 (shaded region) and compared with the values indicated by the exponential fit results for the anomalous accelerations of Pioneer 10 and 11 in Ref. [20] (black dashed and solid lines, respectively).

2.6 Conclusion

In this chapter, an entirely new method to compute spacecraft thermally induced accelerations has been presented and tested. This method was specifically developed to tackle problems where engineering and construction details are scattered and not easily available. Despite its apparent simplicity, the battery of test cases to which it was subjected clearly shows its reliability by ensuring that the errors involved in the simplification of the radiation modelling are well below 10 %.

The parametric analysis that follows the radiation modelling further enhances the trustworthiness of the results. Assumptions are made based on available information, minimising the amount of guessing involved. The width of the resulting interval, for a set probability level, reflect the accuracy of the input data available to construct the model. The more information there is, the narrower the interval will be.

The application of the point-like source method to the Pioneer anomaly produced the first reliable accounting of the thermally induced acceleration on the Pioneer 10 and 11. The obtained acceleration values, as well as the temporal signature, are compatible with the latest descriptions of the detected anomalous acceleration. After our results, it became highly unlikely that the Pioneer anomaly would be explained by anything other than the forces arising from anisotropic thermal radiation.

The confirmation of our results by the ZARM [24] and JPL [25], both using finite-element models, gave the final piece of the puzzle that was missing before the Pioneer anomaly could finally be closed.

References

1. Pioneer Odyssey: Encounter with the Giant (2014), <http://history.nasa.gov/SP-349/ch8.htm>. Accessed 02 Nov 2014
2. NASA Solar System Exploration Multimedia Gallery (2014), http://solarsystem.nasa.gov/multimedia/display.cfm?Category=Spacecraft&IM_ID=16348. Accessed 02 Nov 2014

3. NASA Solar System Exploration Multimedia Gallery (2014), http://solarsystem.nasa.gov/multimedia/display.cfm?IM_ID=2903. Accessed 02 Nov 2014
4. The Pioneer Missions (2014), <http://www.nasa.gov/centers/ames/missions/archive/pioneer.html>. Accessed 02 Nov 2014
5. J. Anderson, P. Laing, E. Lau, A. Liu, M. Nieto, S.G. Turyshev, Study of the anomalous acceleration of Pioneer 10 and 11. *Phys. Rev. D* **65**(8), 082004 (2002). doi:[10.1103/PhysRevD.65.082004](https://doi.org/10.1103/PhysRevD.65.082004)
6. J. Anderson, P. Laing, E. Lau, A. Liu, M. Nieto, S.G. Turyshev, Indication, from Pioneer 10/11, Galileo, and Ulysses data, of an apparent anomalous, weak, long-range acceleration. *Phys. Rev. Lett.* **81**(14), 2858–2861 (1998). doi:[10.1103/PhysRevLett.81.2858](https://doi.org/10.1103/PhysRevLett.81.2858)
7. E. Murphy, Prosaic explanation for the anomalous accelerations seen in distant spacecraft. *Phys. Rev. Lett.* **83**(9), 1890 (1999). doi:[10.1103/PhysRevLett.83.1890](https://doi.org/10.1103/PhysRevLett.83.1890)
8. J. Katz, Comment on indication, from Pioneer 10/11, Galileo, and Ulysses data, of an apparent anomalous, weak, long-range acceleration. *Phys. Rev. Lett.* **83**(9), 1892 (1999). doi:[10.1103/PhysRevLett.83.1892](https://doi.org/10.1103/PhysRevLett.83.1892)
9. O. Bertolami, J. Páramos, A mission to test the Pioneer anomaly: estimating the main systematic effects. *Int. J. Mod. Phys. D* **16**, 1611 (2007). doi:[10.1142/S0218271807011000](https://doi.org/10.1142/S0218271807011000)
10. L. Scheffer, Conventional forces can explain the anomalous acceleration of Pioneer 10. *Phys. Rev. D* **67**(8), 084021 (2003). doi:[10.1103/PhysRevD.67.084021](https://doi.org/10.1103/PhysRevD.67.084021)
11. O. Bertolami, J. Páramos, The Pioneer anomaly in the context of the braneworld scenario. *Class. Quantum Gravity* **21**(13), 3309–3321 (2004). doi:[10.1088/0264-9381/21/13/013](https://doi.org/10.1088/0264-9381/21/13/013)
12. J.R. Brownstein, J.W. Moffat, Gravitational solution to the Pioneer 10/11 anomaly. *Class. Quantum Gravity* **23**(10), 3427–3436 (2006). doi:[10.1088/0264-9381/23/10/013](https://doi.org/10.1088/0264-9381/23/10/013)
13. M.-T. Jaekel, S. Reynaud, Post-Einsteinian tests of linearized gravitation. *Class. Quantum Gravity* **22**(11), 2135–2157 (2005). doi:[10.1088/0264-9381/22/11/015](https://doi.org/10.1088/0264-9381/22/11/015)
14. O. Bertolami, T. Harko, F.S.N. Lobo, Extra force in f(R) modified theories of gravity. *Phys. Rev. D* **75**(10), 104016 (2007). doi:[10.1103/PhysRevD.75.104016](https://doi.org/10.1103/PhysRevD.75.104016)
15. S.G. Turyshev, V.T. Toth, The Pioneer anomaly. *Living Rev. Relativ.* **13**, 4 (2010). doi:[10.12942/lrr-2010-4](https://doi.org/10.12942/lrr-2010-4)
16. O. Bertolami, P. Vieira, Pioneer anomaly and the Kuiper Belt mass distribution. *Class. Quantum Gravity* **23**(14), 4625–4635 (2006). doi:[10.1088/0264-9381/23/14/005](https://doi.org/10.1088/0264-9381/23/14/005)
17. C.B. Markwardt, Independent Confirmation of the Pioneer 10 Anomalous Acceleration (2002), arXiv:[gr-qc/0208046v1](https://arxiv.org/abs/gr-qc/0208046)
18. A. Levy, B. Christophe, P. Bério, G. Métris, J.M. Courty, S. Reynaud, Pioneer 10 Doppler data analysis: disentangling periodic and secular anomalies. *Adv. Space Res.* **43**(10), 1538–1544 (2009). doi:[10.1016/j.asr.2009.01.003](https://doi.org/10.1016/j.asr.2009.01.003)
19. V. Toth, Independent analysis of the orbits of Pioneer 10 and 11. *Int. J. Mod. Phys. D* **18**(05), 717–741 (2009). doi:[10.1142/S0218271809014728](https://doi.org/10.1142/S0218271809014728)
20. S.G. Turyshev, V.T. Toth, J. Ellis, C.B. Markwardt, Support for temporally varying behavior of the Pioneer anomaly from the extended Pioneer 10 and 11 Doppler data sets. *Phys. Rev. Lett.* **107**(8) (2011). doi:[10.1103/PhysRevLett.107.081103](https://doi.org/10.1103/PhysRevLett.107.081103)
21. O. Bertolami, F. Francisco, P.J.S. Gil, J. Páramos, Thermal analysis of the Pioneer anomaly: a method to estimate radiative momentum transfer. *Phys. Rev. D* **78**(10), 103001 (2008). doi:[10.1103/PhysRevD.78.103001](https://doi.org/10.1103/PhysRevD.78.103001)
22. O. Bertolami, F. Francisco, P.J.S. Gil, J. Páramos, Estimating radiative momentum transfer through a thermal analysis of the Pioneer anomaly. *Space Sci. Rev.* **151**(1–3), 75–91 (2010). doi:[10.1007/s11214-009-9589-3](https://doi.org/10.1007/s11214-009-9589-3)
23. F. Francisco, O. Bertolami, P.J.S. Gil, J. Páramos, Modelling the reflective thermal contribution to the acceleration of the Pioneer spacecraft. *Phys. Lett. B* **711**(5), 337–346 (2012). doi:[10.1016/j.physletb.2012.04.034](https://doi.org/10.1016/j.physletb.2012.04.034)
24. B. Rievers, C. Lämmerzahl, High precision thermal modeling of complex systems with application to the flyby and Pioneer anomaly. *Ann. Phys.* **523**(6), 439–449 (2011). doi:[10.1002/andp.201100081](https://doi.org/10.1002/andp.201100081)

25. S.G. Turyshev, V. Toth, G. Kinsella, S.-C. Lee, S.M. Lok, J. Ellis, Support for the thermal origin of the Pioneer anomaly. *Phys. Rev. Lett.* **108**(24), 241101 (2012). doi:[10.1103/PhysRevLett.108.241101](https://doi.org/10.1103/PhysRevLett.108.241101)
26. O. Bertolami, F. Francisco, P.J.S. Gil, J. Páramos, Modeling the nongravitational acceleration during Cassini's gravitation experiments. *Phys. Rev. D* **90**(4), 042004 (2014). doi:[10.1103/PhysRevD.90.042004](https://doi.org/10.1103/PhysRevD.90.042004)
27. B.T. Phong, Illumination for computer generated pictures. *Commun. ACM* **18**(6), 311–317 (1975). doi:[10.1145/360825.360839](https://doi.org/10.1145/360825.360839)
28. V. Toth, S.G. Turyshev, Pioneer anomaly: evaluating newly recovered data. *AIP Conf. Proc.* **977**, 264–283 (2008). doi:[10.1063/1.2902790](https://doi.org/10.1063/1.2902790)

Trajectory Anomalies in Interplanetary Spacecraft
A Method for Determining Accelerations Due to Thermal
Emissions and New Mission Proposals

Francisco, F.

2015, XVII, 87 p. 27 illus., 3 illus. in color., Hardcover

ISBN: 978-3-319-18979-6